

1 Revision 1

2

3 Word Count: 4140

4

5 **A multi-methodological study of the bastnäsite-synchysite polysomatic series: Tips and tricks of**
6 **polysome identification and the origin of syntactic intergrowths**

7

8 Roberto Conconi¹, Patrizia Fumagalli², Giancarlo Capitani^{1*}

9

10 ¹Dipartimento di Scienze dell'Ambiente e della Terra, Università degli Studi di Milano-Bicocca, Piazza
11 della Scienza 4, 20126 – Milano

12

13 ²Dipartimento di Scienze della Terra Ardito Desio, Università degli Studi di Milano, Via Botticelli 23,
14 20133 – Milano

15

16 *corresponding author: giancarlo.capitani@unimi.it

17

18 Keywords: Raman spectroscopy, electron backscattered diffraction, transmission electron microscopy,
19 bastnäsite, synchysite, parisite, polysomatism.

20

21

22

Abstract

23

24 In this paper, we evaluated the potentialities of Raman spectroscopy and electron backscattered
25 diffraction (EBSD) in the microscopic characterization of Ca-REE fluorcarbonates (CRFC) belonging
26 to the bastnäsite-synchysite series to provide a “road map” for further investigations with transmission
27 electron microscopy (TEM). EBSD was effective in establishing the sample orientation, setting up the
28 oriented cuts, and ascertaining the effective syntactic relationship among all the detected CRFC phases;
29 however, it failed to distinguish between different polysomes. On samples with different orientations
30 that were preventively ascertained by EBSD and characterized by scanning electron microscopy (SEM)
31 coupled with energy dispersive X-ray spectroscopy (EDS), performing micro-Raman spectroscopy
32 allows distinguishing between polysomes based on the differences in intensity and position of the
33 symmetric stretching vibration (ν_1) of the carbonate group (CO_3^{2-}) in the region around 1080–1099 cm^{-1}
34 ¹. However, as evidenced by TEM-EDS, what appears as a homogeneous polysome in backscattered
35 electrons (BSE) images may be a disordered intergrowth of compositional faults with a bulk

36 composition being matched with that of a real polysome only by accident. Therefore, we conclude that
37 the Raman signal is sensitive to different Ca/(Ca+REE) ratios but not to any ordered distribution of Ca-
38 poor and Ca-rich lamellae within the analyzed volume, making the unambiguous identification of a
39 polysome tricky. Finally, several ordered polysomes were detected at the TEM scale, including a B_2S
40 and a long-range polytype with a 32 nm repeat distance along c . The possible implications of the
41 detected microstructure for ore mineral formation are discussed.

42

43

44

Introduction

45 The Ca-REE fluorcarbonates (hereafter CRFC) are important minerals for at least two (apparently)
46 distant reasons, one tied to fundamental research and the other to critical raw materials. Indeed, from a
47 crystallographic point of view, CRFC form a polysomatic series (Veblen, 1991) with bastnäsite
48 $[\text{REE}(\text{CO}_3)\text{F}]$ and synchysite $[\text{CaREE}(\text{CO}_3)_2\text{F}]$ as the end members (Fig. 1). Accordingly, intermediate
49 terms can be described by bastnäsite (B) and synchysite (S) modules (B_nS_m) and their composition
50 calculated as $[\text{REE}(\text{CO}_3)\text{F}]_m \cdot [\text{CaREE}(\text{CO}_3)_2\text{F}]_n$ (Donnay & Donnay, 1953). Intermediate terms of the
51 series are parisite $[\text{CaREE}_2(\text{CO}_3)_3\text{F}_2]$ (or BS) and röntgenite $[\text{Ca}_2\text{REE}_3(\text{CO}_3)_5\text{F}_3]$ (or BS_2). Possible
52 additional intermediate polysomes have been described by high-resolution transmission electron
53 microscopy (HRTEM) studies (van Landuyt & Amelinckx, 1975; Wu et al., 1998; Meng et al., 2001a,
54 b, 2002; Ciobanu et al., 2017; Capitani, 2019, 2020; Zeug et al., 2021). Moreover, the layer sequence
55 within a polysome may be different: a given layer (B or S) may be differently rotated with respect to
56 the ordered sequence, giving rise to polytypism and polytypic disorder as in micas (Banfield et al.,
57 1994). Finally, within a polysome, B and S layers may exchange relative positions giving rise to
58 polymorphism (Capitani, 2019).

59 On the other hand, bastnäsite and synchysite are the most important ore minerals for Ce, La, Nd, and Y.
60 The demand for these REEs has spiked in recent years due to their increasing usage in numerous high-
61 technology applications, including electronics and green technologies. For instance, Ce oxide (Ce_2O_3)
62 is used in catalytic converters, La and Nd are used in the manufacturing of hybrid and electric motors
63 and rotors of wind turbines, Nd compounds are used for the manufacturing of the most powerful
64 permanent magnets occurring in microphones, speakers and hard disks, and synthetic Y garnet
65 ($\text{Y}_3\text{Al}_2\text{O}_{12}$) is used in filters for microwaves, acoustic transmitters and transducers, LEDs, lasers and
66 even as gems (e.g., Goonan, 2011; Charalampides et al., 2015).

67 In nature, CRFC rarely occur as single crystals. Commonly, they form microscale syntactic
68 (crystallographically oriented) intergrowths (Donnay & Donnay, 1953) of different
69 polysomes/polytypes, often with stacking faults at the nanoscale. Due to this recurrent microstructure,
70 definitive structural analyses by single-crystal X-ray diffraction (SCXRD) have been achieved
71 relatively recently and only for some basic polysomes, namely bastnäsite-(Ce) (Ni et al., 1993),
72 synchysite-(Ce) (Wang et al., 1994), and parisite-(Ce) (Ni et al., 2000). Apart from these fortunate
73 cases, for most of the occurrences with intergrowths at the microscale, reliable structural analysis can
74 only be performed via TEM.

75 Regarding SEM-EDS analysis, which is a relatively faster characterization technique compared to
76 HRTEM, syntactic intergrowths can be revealed by the average atomic number (Z) contrast in BSE
77 images. However, no orientation relationships can be obtained, and submicroscopic intergrowths may
78 be hidden and merged into a uniform-gray-tone microscopic band. Along the same lines, microprobe
79 analysis, whose spatial resolution is on the order of a few micrometers, in the case of submicroscopic
80 lamellae within the analyzed volume can only give an average composition that may accidentally
81 match the composition of a potential polysome.

82 Raman spectroscopy is another relatively faster characterization technique that has been so far poorly
83 exploited in these minerals. Ce-dominant CRFC has been investigated by Frost and Dickfos (2007),
84 Guastoni et al. (2009), and recently by Zeug et al. (2021), sometimes providing contrasting results.
85 Raman spectroscopy has a spatial resolution comparable to microprobe analysis, and according to Zeug
86 et al. (2021), it can distinguish between some basic polysomes; however, the influence of
87 submicroscopic lamellae on the Raman response is not clear. On the other hand, electron backscattered
88 diffraction (EBSD) has, in principle, a spatial resolution that is much better (tens of nm) than that of the
89 techniques mentioned above, and it may give orientation relationship information; however, its
90 capability to distinguish between different CRFC has never been tested.

91 In this paper, we investigate well-characterized CRFC from Mount Malosa (Malawi) (Guastoni et al.,
92 2009, 2010; Capitani, 2019) by combining Raman spectroscopy and EBSD—the latter applied, as far
93 as we know, for the first time to CRFC—to evaluate the potentialities of these two methodologies in
94 the characterization of this material at a microscopic scale and provide a “road map” for further focused
95 investigation, aiming, for instance, to determine new polysomes with TEM.

96 Investigations at the microscopic and submicroscopic scale of CRFC (or any other ore mineral) may
97 prove to be important for the understanding of the ore mineral formation and possibly for the
98 improvement of downstream processing and REE recovery.

99 100 **Samples and Methods**

101 102 **Samples and sample preparation**

103
104 The samples studied in this work come from Mount Malosa, Malawi, and were previously described by
105 Guastoni et al. (2009, 2010) and Capitani (2019). All CRFC samples display a yellowish-reddish color
106 and are associated with aegirine (Fig. 2). Before instrumental investigations, all samples were
107 embedded in epoxy resin and then cut in parallel either to main or generic orientations, first roughly

108 determined by visual inspection of the crystal habit, then following the EBSD results (see ahead): i)
109 sample 9c1 sectioned parallel to the x-y (z-axis perpendicular to the section); ii) samples 3 and 9c2
110 sectioned parallel to the y-z plane (z-axis in the plane of the section); iii) sample 9b and 6 sectioned
111 parallel to a generic orientation (z-axis at a high angle and a low angle to the section, respectively). All
112 samples were mechanically polished with a rotational system using alumina with a nominal grain
113 diameter of 0.3 μm as the last polishing step. Those designated for EBSD investigations were further
114 etch-polished with a Saphir Vibro vibratory polishing device using 0.06 μm colloidal silica. Electron
115 transparent TEM mounts were prepared from sample 9c2, i.e., the one with the optimal orientation to
116 study syntactic intergrowths, which alternate along the c-axis (Donnay & Donnay, 1953). After SEM
117 analyses, a double-polished 30- μm thick section stuck with Attack® to a glass slide was obtained from
118 the same samples. Copper rings, 3 mm in diameter, were stuck with Araldite® on the selected sample
119 areas, removed from the glass along with the attached minerals by acetone dissolution of the Attack,
120 and ion-milled down to electron transparency by a Gatan PIPS II Cool instrument. All samples were
121 carbon coated with a 20 nm C-film before SEM observations and with a 5 nm C-film before EBSD and
122 TEM investigations. The C-film was removed before Raman spectroscopy to avoid fluorescence.

123 124 **Instrumental analyses**

125
126 SEM imaging and analysis were performed at the Platform of Microscopy of the University of Milano-
127 Bicocca (PMiB) with a field emission gun (FEG) SEM Zeiss Gemini 500, operating at 20 keV and
128 equipped with a Bruker XFlash EDS. The standardless method and ZAF correction were used for semi-
129 qualitative analysis. EBSD investigations were performed with a high-resolution Bruker eFlash
130 detector mounted on the same FEG-SEM Zeiss Gemini 500.

131 The Raman spectroscopy analyses were performed at the Department of Earth Science “Ardito Desio”
132 of the University of Milan. The analyses were obtained at room temperature using a LabRAM HR

133 Evolution spectrometer. The system is equipped with an Olympus BX series optical microscope, a
134 diffraction grating of 1800 grooves per millimeter, and a Si-based Peltier-cooled CCD detector. Spectra
135 were excited with the 633 nm emission of a He-Ne laser and were obtained using a 100x objective with
136 an acquisition time of 3x30 s. All the spectra were collected close to SEM analysis spots. Fitting of
137 Raman spectra was done after background correction assuming Lorentzian band shapes. The system
138 was calibrated using the 520.7 cm^{-1} line of a silicon wafer. A $\frac{1}{2} \lambda$ wave plate was used to polarize the
139 light. Spectra were obtained with two different polarization directions of the incident electron field
140 vector (\mathbf{E}): $\mathbf{E} \perp z$ and $\mathbf{E} // z$ in samples 3 and 9c2; $\mathbf{E} // y$ and $\mathbf{E} \approx // x$ in sample 9c1.

141 TEM observations were performed at the PMiB with a Jeol JEM2100Plus, supplied with a LaB_6 source
142 and operating at 200kV. The instrument is equipped with an Oxford EDS system and a Gatan Rio
143 CMOS camera. The Digital Micrograph® software (Gatan) was used for image acquisition and
144 processing. The HRTEM filter developed by D.R.G Mitchell (2007) was employed to reduce the
145 inelastic scattering in HR images. EDS analyses were collected and quantified with Aztec (Oxford)
146 software using the standardless method and correction for absorption. The method developed by Van
147 Cappellen and Doukhan (1994) was used to estimate the thickness of the TEM mount at the point
148 analysis spots. The estimated beam diameter at the sample surface was 3.5 nm.

149

150

Results

151

Microstructure and composition (SEM-EDS results)

152

153
154 Syntactic intergrowths in CRFC were first studied by SEM-EDS for a first glimpse of the
155 microstructure and the chemical variability at a microscopic scale. As expected, BSE images
156 demonstrate the parallel banding typical of CRFC syntactic intergrowths (Fig. 3). EDS spot analyses
157 were acquired within bands showing homogeneous gray tones. These analyses align with those

158 acquired by wave dispersive X-ray spectroscopy (WDS) in a previous study of different crystals from
159 the same samples (Guastoni et al. 2009). Therefore, this indicates that EDS is sufficiently accurate for
160 the identification of microscopic CRFC polysomes; at the same time, it is much faster than WDS
161 (Table 1). The EDS analyses display an inverse correlation of the Ca/(Ca+REE) ratio with the BSE
162 intensity (brightness) of the bands. All the measured phases are Ce-dominant and contain La and Nd as
163 other major REEs, whereas Sm, Y, Pr, and Gd may be present as minor components. An exception is
164 represented by synchysite, where Y is more abundant than La and Nd. Fluorine is underestimated in
165 SEM-EDS analyses due to its tendency to diffuse under the influence of a highly focused electron
166 beam. Overall, the chemical compositions of lamellae span from bastnäsite to synchysite depending on
167 the sample and align almost continuously between röntgenite, parisite, and the B_2S polysome (Fig. 3).
168 In particular, other than compositions close to bastnäsite, parisite, röntgenite and synchysite [ideal
169 Ca/(Ca+REE) ratio of 0, 0.33, 0.40 and 0.50, respectively], lamellae with Ca/(Ca+REE) of 0.23 and
170 0.27, which are close to the B_2S polysome (0.25), and lamellae with a Ca/(Ca+REE) of 0.36 (Table 1S,
171 in the supplementary materials) have been often encountered. Moreover, a few analyses with a
172 Ca/(Ca+REE) ratio of 0.20, theoretically corresponding to polysomes B_3S , 0.14 (B_5S), and 0.29
173 (intermediate between parisite and B_2S), have also been collected. At this level, it is unknown whether
174 or not the determined compositions correspond to ordered polysomes or arise from disordered
175 intergrowths at the nanoscale.

176
177 **Lamellae orientation (EBSD results)**
178

179 EBSD analyses were undertaken to i) establish the initial orientation of the samples, ii) align the
180 sample for oriented cuts in view of both Raman and TEM investigations, and iii) test the method's
181 capability to discriminate different polysomes. Unsurprisingly, the EBSD results allowed us to
182 establish the sample orientation, set up the oriented cuts, and ascertain the effective syntactic

183 relationship among all the detected CRFC phases; however, it failed to distinguish between different
184 polysomes (Fig. 4). This drawback can be easily understood if one considers that electron diffraction
185 (similar to X-ray diffraction) is dominated by heavy atoms and that CRFC of the *BS* series, although
186 monoclinic, have a hexagonal stacking of heavy atoms (Ca and REE) that is identical to that in
187 bastnasite, the only effective hexagonal term (Ni et al., 1993, 2000; Wang, 1994). Different polysomes
188 can be actually distinguished through EBSD maps if EDS chemical information is acquired at the same
189 time and if the map is elaborated with both contributions (50% EDS and 50% EBSD). In this case, the
190 syntactic intergrowths are correctly indexed, but the method loses interest since EDS has a spatial
191 resolution (few μm) two orders of magnitude worse than EBSD (tens of nm).

192 **Raman spectroscopy**

193 Raman spectroscopy analyses were taken on lamellae previously characterized by SEM-EDS in an
194 attempt to correlate the Raman signal with the chemical composition, aiming to distinguish between
195 different polysomes. Peak assignment was done according to White (1974), Buzgar and Apopei (2009),
196 and Zeug et al. (2021). In particular, the following internal vibrational modes of the carbonate group
197 were identified: i) symmetric stretching [$\nu_1(\text{CO}_3)$]; ii) out-of-plane bending [$\nu_2(\text{CO}_3)$]; iii)
198 antisymmetric stretching [$\nu_3(\text{CO}_3)$]; iv) in-plane bending [$\nu_4(\text{CO}_3)$] (Table 2 and Fig. 5).

201 Since the intensity of Raman peaks changes in relation to both crystal orientation and laser polarization,
202 four different configurations whose details and related Porto's notations (Damen et al., 1966) are
203 reported in Table 3 were investigated. The highest intensity of the $\nu_1(\text{CO}_3)$ stretching vibration was
204 obtained in sample 9c2 with the $x \begin{pmatrix} z \\ y \end{pmatrix} \bar{x}$ configuration. Conversely, the lowest intensity was obtained
205 with the $z \begin{pmatrix} y \\ x \end{pmatrix} \bar{z}$ setting (Fig. 6). Orientation of the polysomes and laser polarization influence the
206 intensity of the bands only and not their positions.

207 In agreement with Zeug et al. (2021), we found that the $\nu_4(\text{CO}_3)$ in-plane bending is in the range of
208 $665\text{--}754\text{ cm}^{-1}$ and seems separated into two sub-regions. The $\nu_2(\text{CO}_3)$ out-of-plane bending is around
209 870 cm^{-1} . The $\nu_3(\text{CO}_3)$ antisymmetric stretching is around 1440 cm^{-1} and is orientation dependent. The
210 $\nu_1(\text{CO}_3)$ symmetric stretching is around 1100 cm^{-1} and is split into three bands in intermediate
211 polysomes: at $\sim 1081\text{ cm}^{-1}$, $1091\text{--}1095\text{ cm}^{-1}$, and $\sim 1099\text{ cm}^{-1}$, whose relative intensities vary with
212 composition (i.e., Ca/REE ratio, s. also Fig. 15). End members behave somewhat differently: bastnäsite
213 demonstrates only one intense peak at $\sim 1095\text{ cm}^{-1}$ and synchysite two bands at 1081 cm^{-1} and 1099 cm^{-1}
214 (Table 2 and Fig. 7). As observed in Zeug et al. (2021), we also detected other bands at 598, 1564 and
215 1738 cm^{-1} , whose origin was not clarified (Fig. 5).

216

217 **Nanostructure (TEM results)**

218

219 The sample studied by SEM-EDS and Raman spectroscopy with a favorable orientation for the study of
220 syntactic intergrowths (i.e., with the z-axis laying on the observation plane, sample 9c2) was prepared
221 for TEM to elucidate the structural state associated with the encountered compositions. Ordered regions
222 in sample 9c2 are rare and limited to less than $1\text{ }\mu\text{m}$ along the stacking direction. Indeed, the most
223 recurrent microstructure is given by a pervasive occurrence of stacking faults (e.g., Fig. 8a) affecting
224 bastnäsite and parisite, these last by far the most abundant phases detected in the sample (Fig. 8 and 9).
225 Limited regions of B_2S and B_5S showing consistent compositions (Table 2S in the supplementary
226 material) were also detected (Fig. 10), in agreement with SEM-EDS. As for SEM-EDS, a few point
227 analyses with a Ca/(Ca+REE) ratio of 0.29 – unrelated to any basic polysome – were measured by
228 TEM-EDS; however, they could not be connected with the underlying structure/microstructure.
229 Moreover, a long-range polytype with a repeat distance of $\sim 32\text{ nm}$ was also observed (Fig. 11).
230 Conversely, even if SEM-EDS and Raman spectroscopy suggest abundant röntgenite, clear evidence of
231 this polysome has not been confirmed by TEM. Along the same lines, the abundant lamellae with a

232 Ca/(Ca+REE) ratio of 0.36 detected by SEM-EDS (Table 1S) were not detected by TEM. Finally, a
233 new parisite-(Ce) polymorph was detected, distinguished from normal parisite (Ni et al., 2000) and the
234 other polymorphs described by Capitani (2019) by twice the repeat distance along c^* (~56 vs. ~28 Å,
235 respectively), suggesting a repetition of four basic *BS* modules (~14 Å) along the stacking direction
236 (Fig. 12).

237 Even considering that using TEM, it is not possible to explore the whole area explored by SEM and
238 that we could have missed some compositions, our findings seem to indicate that, at least in part, the
239 intermediate compositions detected by SEM-EDS on apparently homogeneous lamellae may result
240 from sub-microscopic compositional faults (polysomatic faults), not resolved in BSE images, matching
241 only by accident the composition of a theoretical polysome.

242 Compositional faults in bastnäsite can only be Ca-rich through the local insertion of vaterite-like slabs,
243 whereas in parisite, they can be either Ca-rich or Ca-poor, i.e., through a bastnäsite-like slabs insertion.
244 As matter of fact, in the studied samples, compositional faults in parisite are mostly Ca-poor. These
245 conclusions are supported by nanoscale EDS analysis and HRTEM imaging (s. also Capitani, 2019).
246 The Ca/(Ca+REE) ratio that is slightly higher than 0 in bastnäsite and lower than 0.33 in parisite (Table
247 2S) can be interpreted in this way.

248 Figure 13 reports bright field (BF) scanning transmission electron microscopy (STEM) images and
249 related compositional line scans across a Ca-poor lamella hosted in parisite and Ca-rich lamellae in
250 disordered bastnäsite. In both cases, a clear inverse correlation between Ca and Ce can be observed.

251 Figure 14 reports an HRTEM image of bastnäsite ($c \sim 10$ Å) including some compositional faults,
252 consistent with B_2S and B_3S single slabs, with a thickness of ~19 and ~24 Å, respectively. The random
253 occurrence of Ca-bearing compositional faults may explain the minor Ca content sometimes detected in
254 bastnäsite and may cause an accidental matching of SEM-EDS analyses with intermediate polysome
255 compositions, causing misinterpretation.

256

257

Discussion and Conclusions

258

Polysome detectability through Raman spectroscopy

259

260
261 According to Raman results, the identification of the basic CRFC is possible through the symmetric
262 $\nu_1(\text{CO}_3)$ stretching vibration at $\sim 1100 \text{ cm}^{-1}$ (Fig. 5). Bastnäsite and synchysite can be easily
263 distinguished from other polysomes by the strong Raman band at 1095 cm^{-1} present in the former and
264 the two bands at 1081 cm^{-1} and 1099 cm^{-1} present in the latter. Parisite, B_2S , and röntgenite all have
265 three different bands at $\sim 1081 \text{ cm}^{-1}$, $\sim 1091\text{--}1095 \text{ cm}^{-1}$ (hereafter 1091 cm^{-1}), and $\sim 1099 \text{ cm}^{-1}$, which
266 only differ in intensity. According to Zeug et al. (2021), the identification of these intermediate
267 polysomes is possible through the $1091 \text{ cm}^{-1}/1081 \text{ cm}^{-1}$ intensity ratio. We found this ratio to decrease
268 linearly with the $\text{Ca}/(\text{Ca}+\text{REE})$ ratio for samples with $\mathbf{E} // z$ and with a parabolic shape for samples
269 with $\mathbf{E} \perp z$ (Fig. 15).

270 The number and position of the symmetric $\nu_1(\text{CO}_3)$ stretching vibration Raman bands depend on the
271 valence and ionic radius (Adler & Kerr, 1963) of the neighboring CO_3^{2-} groups. Actually, two different
272 types of CO_3^{2-} -layers are present in the CRFC structure: those in contact on both sides with CeF-layers
273 (or *e*-layers) and those in contact with one CeF-layer on one side and one Ca-layer (or *g*-layers) on the
274 other side (Donnay & Donnay, 1953). Only (symmetric) *e*-layers are present in bastnäsite (Yang et al.,
275 2008), resulting in one strong band at 1095 cm^{-1} , whereas only (asymmetric) *g*-layers are present in
276 synchysite (Wang et al., 1994), resulting in two different bands at 1081 and 1099 cm^{-1} . Both *e*-layers
277 and *g*-layers are present in intermediate polysomes such as parisite, B_2S , and röntgenite (Ni et al., 1993,
278 2000), leading to a tripartition of the symmetric $\nu_1(\text{CO}_3)$ stretching vibration.

279 The impression gathered after TEM-EDS is that ordered regions in CRFC syntactic intergrowths from
280 Malawi are smaller than expected according to SEM-EDS imaging. Consequently, compositional faults

281 at the nanoscale in bastnäsite and parisite—not resolved in SEM-BSE images—may affect the
282 Ca/(Ca+REE) ratio, which can match the composition of a real polysome only by accident. In light of
283 these results, Raman spectroscopy, whose spatial resolution is $\sim 1 \mu\text{m}$, needs to be critically re-
284 examined. We believe that the Raman signal is sensitive to different abundances of *e*- and *g*-layers in
285 the structure, whose proportions vary with composition and thus also with the polysome, but not to the
286 order of the layers within the analyzed volume. Therefore, whereas Raman spectroscopy could be a
287 valid and faster method to probe the Ca/(Ca+REE) content of fluorcarbonates, it does not appear to be
288 possible to distinguish between ordered and disordered intergrowths with similar compositions.

289

290 **Polysome detectability through electron-beam-related techniques**

291

292 Although the nanoscale disorder can be overlooked, SEM-EDS is the fastest technique for polysome
293 identification. TEM-EDS remains the ultimate technique for polysome identification; however, it is
294 time-consuming and provides only local information. Since most high-resolution TEMs have a limited
295 tilt range, the sample needs to be pre-oriented before preparation; in this case, EBSD can be very
296 useful. In this regard, EBSD can easily distinguish CRFC among other phases and correctly provides
297 their orientation relationship; however, under routine application, it fails to distinguish between
298 different polysomes.

299 At the TEM scale, other than basic CRFC, intermediate polytypes that have not yet been fully
300 described in the literature have been identified. Among these are a B_2S polysome, a 32 nm long-range
301 polytype, and a new parisite polymorph with a double *c* parameter compared to normal parisite.
302 Further investigations are required for a full characterization of all these new structures.

303

304

304 **Implications for REE Ore Formation**

305

306 In principle, under equilibrium crystallization conditions, every single fluid composition falling within

307 the bastnäsite-synchysite series can be accommodated by a proper proportion of *B* and *S* layers;
308 therefore, this situation opposes the simultaneous crystallization of two similar phases of different
309 compositions, as in the well-known case of the alkali feldspar system at high pressure (e.g., Winter,
310 2001) when the fluid composition falls within the miscibility gap, promoting the simultaneous
311 crystallization of a Na-rich and a K-rich feldspar upon cooling.

312 The inability of the system $\text{CeFCO}_3\text{--CaCO}_3$ to form solid solutions was considered a factor explaining
313 the presence of syntactic intergrowths in CRFC (Donnay & Donnay 1953). One crystal precipitates
314 until the conditions in the solution have changed sufficiently for the next compound to separate out,
315 which then crystallizes on the original crystal. Since the two species alternate, periodic and
316 discontinuous changes in the conditions of the system must be postulated. Variations in the $a\text{Ca}^{2+}$,
317 $a\text{REE}^{3+}$, $a(\text{CO}_3)^{2-}$, $a\text{F}^-$, and *T* of the solution may well be the controlling factors during crystal growth
318 (Gysi & Williams-Jones, 2015). Therefore, it appears that syntactic intergrowths are the equivalent of
319 zoning in crystal-chemical systems that cannot form solid solutions.

320 Bastnäsite-(Ce) and synchysite-(Ce) both occur at Mt. Malosa (Malawi) but in separate samples, i.e.,
321 they are never observed in contact. Moreover, the chemical composition is remarkably different in
322 terms of REE partitioning, i.e., synchysite is richer in Y (and poorer in Ce, La, and Nd) than bastnäsite
323 and all the other intermediate terms (Table 1 and 1S). This could indicate that synchysite formed under
324 different time-space physicochemical conditions than the other polysomes.

325 The most recurrent microstructure in Mt. Malosa CRFC is represented by rhythmic parisite-bastnäsite
326 intergrowths with a number of more or less ordered intermediate polysomes. This microstructure is
327 similar to that of the Olympic Dam Australia deposit (Ciobanu et al., 2022); however, a clear trend of
328 compositions varying gradually from a basic polysome to the next through disordered domains has not
329 been observed at Mt. Malosa. The observed microstructure suggests a primary growth mechanism in
330 which fluorcarbonates crystallize from a fluid close to thermodynamic equilibrium whose conditions

331 quickly and repeatedly crossed the parisite–bastnäsite stability boundary, rather than a stepwise
332 approach toward thermodynamic equilibrium.

333 According to Secco et al. (2007), the crystallization of CRFC at Mount Malosa occurred at ~1 kbar and
334 300–400 °C. These data are fully consistent with the mineral–fluid stability diagrams for the Ca–REE–
335 C–O–H–F system of Gysi and Williams-Jones (2015), from which it appears how the boundary
336 between parisite–bastnäsite, which has a negative slope on the $\log aF^-$ vs. $\log a(CO_3)^{2-}$ diagram, can be
337 easily crossed after small variations of either $a(CO_3)^{2-}$ or aF^- , thus representing the most probable
338 reasons for the departure from equilibrium conditions. It should be noted, however, that an increase of
339 $a(CO_3)^{2-}$ in the fluid (or aF^- , or both), for instance, would cause the crystallization of parisite at the
340 expense of bastnäsite (Fig. 16). The protracting of this situation, however, would cause an increase of
341 $aREE^{3+}$ in the remaining fluid, therefore realizing the conditions for the crystallization of bastnäsite (or
342 some other polysomes poorer in Ca than parisite). In other words, the crystallization itself may induce
343 rhythmic changes in the fluid composition at the crystallization front leading to syntactic intergrowths,
344 which therefore appear as a rather unavoidable fact in Ca-REE fluorcarbonates.

345

346

Acknowledgments

347

348 This study was supported by MIUR (Italian Ministry of University and Research) – Dipartimenti di
349 Eccellenza 2018–2022 “Study the past and the present to understand how the climate will change in the
350 future” and by FAQC (University Competitive Funds) 2022 “Carbon REE-Cycle”. Alessandro
351 Guastoni provided the samples. Lucrezia Commissario and Walter Isola performed preliminary SEM-
352 EDS investigations. Andrea Lucotti is greatly acknowledged for the discussion of Raman’s results.
353 Constructive comments by Fernando Nieto and Bernad Grobéty greatly improved the manuscript.

354

355

References

- 356
357 Adler, H.H., and Kerr, P.F. (1963) Infrared spectra, symmetry and structure relations of some carbonate
358 minerals. *American Mineralogist*, 48, 839–853.
- 359 Banfield, J.F., Bailey, S.W., and Barker, W.W. (1994) Polysomatism, polytypism, defect
360 microstructure, and reaction mechanisms in regularly and randomly interstratified serpentine and
361 chlorite. *Contributions to Mineralogy and Petrology*, 117, 137-150.
- 362 Buzgar, N., and Apopei, A.I. (2009) The Raman study of certain carbonates. *Geologie*, 55, 97-112.
- 363 Capitani, G. (2019) HRTEM investigation of bastnaesite–parisite intergrowths from Mount Malosa
364 (Malawi): Ordered sequences, polysomatic faults, polytypic disorder, and a new parisite-(Ce)
365 polymorph. *European Journal of Mineralogy*, 31, 429-442.
- 366 Capitani, G. (2020) Synchysite-(Ce) from Cinquevalli (Trento, Italy): Stacking Disorder and the
367 Polytypism of (Ca,REE)-Fluorcarbonates. *Minerals*, 10, 77.
- 368 Charalampides, G., Vatalis, K., Apostoplos, B., and Ploutarch-Nikolas, B. (2015) Rare earth elements:
369 Industrial applications and economic dependency of Europe. *Procedia Economics and Finance*, 24,
370 126–135.
- 371 Ciobanu, C.L., Kontonikas-Charos, A., Slattery, A., Cook, N.J., Ehrig, K., and Wade, B.P. (2017)
372 Short-range stacking disorder in mixed-layer compounds: A HAADF STEM study of bastnäsite-
373 parisite intergrowth. *Minerals*, 7, 277.
- 374 Ciobanu, C.L., Cook, N.J., Slattery, A.D., Ehrig, K., and Liu, W.Y. (2022) Nanoscale intergrowths in
375 the bastnäsite–synchysite series record transition toward thermodynamic equilibrium. *MRS*
376 *Bulletin*, 47, 250-257.
- 377 Damen, T.C., Porto, S.P.S., and Tell, B. (1966) Raman Effect in Zinc Oxide. *Physical Review*, 142,
378 570-574.
- 379 Donnay, G., and Donnay, J.D.H. (1953) The crystallography of bastnäsite, parisite, röntgenite and

- 380 synchysite. *American Mineralogist*, 38, 932–963.
- 381 Frost, R.L., and Dickfos, M.J. (2007) Raman spectroscopy of halogen-containing carbonates. *Journal of*
382 *Raman Spectroscopy*, 38, 1516–1522.
- 383 Goonan, T.G. (2011) Rare earth elements—End use and recyclability. U.S. Geological Survey,
384 Scientific Investigations Report, 2011-5094.
- 385 Guastoni, A., Nestola, F., and Giaretta, A. (2009) Mineral chemistry and alteration of rare earth
386 element (REE) carbonates from alkaline pegmatites of Mount Malosa, Malawi. *American*
387 *Mineralogist*, 94, 1216–1222.
- 388 Guastoni, A., Kondo, D., and Nestola, F. (2010) Bastnäsite-(Ce) and parisite-(Ce) from Mt. Malosa,
389 Malawi. *Gems & Gemology*, 46, 42–47.
- 390 Gysi, A.P. and Williams-Jones, A.E. (2015) The thermodynamic properties of bastnäsite-(Ce) and
391 parisite-(Ce). *Chemical Geology*, 392, 87–101.
- 392 Meng, D., Wu, X., Mou, T., and Li, D. (2001a) Determination of six new polytypes in parisite-(Ce) by
393 means of high-resolution electron microscopy. *Mineralogical Magazine*, 65, 797–806.
- 394 Meng, D., Wu, X., Mou, T., and Li, D. (2001b) Microstructural investigation of new polytypes of
395 parisite-(Ce) by high-resolution transmission electron microscopy. *The Canadian Mineralogist*, 39,
396 1713–1724.
- 397 Meng, D., Wu, X., Han, Y., and Meng, X. (2002) Polytypism and microstructures of the mixed-layer
398 member B_2S , $CaCe_3(CO_3)_4F_3$ in the bastnäsite-(Ce)-synchysite-(Ce) series. *Earth and Planetary*
399 *Sciences Letters*. 203, 817-828.
- 400 Mitchell, D.R. (2007) HRTEM filter. Digital Micrograph Script Database (ver. 2019.11.01) (Online).
401 Available: http://www.dmscripting.com/hrtem_filter.html FELMI. Graz University of Technology,
402 Austria.
- 403 Ni, Y., Hughes, J.M., and Mariano, A.N. (1993) The atomic arrangement of bastnäsite (Ce), $Ce(CO_3)F$,

- 404 and structural elements of synchysite-(Ce), röntgenite-(Ce), and parisite-(Ce). American
405 Mineralogist, 78, 415-418.
- 406 Ni, Y., Post, J.E., and Hughes, J.M. (2000) The crystal structure of parisite-(Ce), $Ce_2CaF_2(CO_3)$.
407 American Mineralogist, 85, 251–258.
- 408 Secco, L., Guastoni, A., Nestola, F., Redhammer, G.J., and Dal Negro, A. (2007) Crystal chemistry of
409 aegirine as indicator of P-T conditions. Mineralogical Magazine, 71, 249–255.
- 410 Van Cappellen, E., and Doukhan, J.C. (1994) Quantitative transmission X-ray microanalysis of ionic
411 compounds. Ultramicroscopy, 53, 343-349.
- 412 Van Landuyt, J., and Amelinckx, S. (1975) Multiple beam direct lattice imaging of new mixed-layer
413 compounds of the bastnäsite-synchysite series. American Mineralogist, 60, 351–358.
- 414 Veblen, D.R. (1991) Polysomatism and polysomatic series: A review and applications. American
415 Mineralogist, 76, 801–826.
- 416 Wang, L., Ni, Y., Hughes, J.M., Bayliss, P., and Drexler J.W. (1994) The atomic arrangement of
417 synchysite-(Ce), $CeCaF(CO_3)_2$. The Canadian Mineralogist, 32, 865–871.
- 418 White, W.B. (1974) The carbonate minerals. In V.C. Farmer, Ed., The infrared spectra of minerals, p.
419 227-284. Mineralogical Society, London.
- 420 Winter, J.D. (2001) An introduction to igneous and metamorphic petrology, 786 p. Prentice Hall, New
421 Jersey.
- 422 Wu, X., Meng, D., Pan, Z., and Yang, G. (1998) Transmission electron microscope study of new,
423 regular, mixed-layer structures in calcium-rare earth fluorcarbonate minerals. Mineralogical
424 Magazine, 62, 55–64.
- 425 Yang, H., Dembowski, R.F., Conrad, P.G., and Downs, R.T. (2008) Crystal structure and Raman
426 spectrum of hydroxyl-bastnasite-(Ce), $CeCO_3(OH)$. American Mineralogist, 93, 698-701.
- 427 Zeug, M., Nasdala, L., Ende, M., Habler, G., Hauzenberger, C., Chanmuang, C., Škoda, R., Topa, D.,

428 Wildner, M., and Wirth, R. (2021) The parisite–(Ce) enigma: challenges in the identification of
429 fluorcarbonate minerals. *Mineralogy and Petrology*, 115, 1-19.

430

431

List of table and figure captions

432

433 Table 1. Comparison between semi-quantitative (EDS) and quantitative (EMPA) analyses of bastnäsite,
434 parisite and synchysite.

435

436 Table 2. Summary of the (CO₃) vibrational modes in CRFC and their positions as determined in this
437 study.

438

439 Table 3. Crystal and laser beam settings and related Porto's notations.

440

441 Figure 1. Drawings of the basic CRFC structures showing the different building layers (and related
442 names in different coding systems; further details in Capitani, 2019) stacked along the **c**-axis (vertical).

443

444 Figure 2. a) Reflected light optical micrograph of sample 9c2 showing the typical banding contrast due
445 to syntactic intergrowths. The black areas are voids. On the right, stereomicroscopy photos of samples
446 9c2 and 9c1 with their respective orientations obtained through EBSD. Red circles represent the
447 positions where the 3 mm copper rings were placed to extract TEM samples.

448

449 Figure 3. Left: SEM-BSE image of sample 9c2 showing the syntactic intergrowths of different CRFC
450 minerals. The compositional contrast is consistent with the average Z-number of the analyzed phases:
451 dark gray corresponds to röntgenite, light gray to bastnäsite and intermediate gray tones to parisite and

452 other intermediate polysomes (black areas are voids). Right: Ca/(Ca+REE) vs. REE/(Ca+REE) plot of
453 EDS analyses (blue dots) along with ideal compositions of basic and theoretical polysomes (orange
454 squares). Most of the analyzed lamellae show a composition within the B_2S -röntgenite join.
455 Compositions deviating from the ideal ratios (but also those matching the ideal ratios!) may be due to
456 compositional faults (see TEM section).

457

458 Figure 4. a) BSE image with superposed EBSD phase map of sample 9c2. The legend reports the
459 coloring scheme of all phases considered by the program. The EBSD system indexes correctly
460 bastnäsite (Bas, red) but fails to correctly identify röntgenite (Roe, blue), which is mostly
461 misinterpreted as parisite (green). As a matter of fact, the electron backscattered patterns of röntgenite
462 (b) and parisite (c), are geometrically indistinguishable, leading to ambiguous zone-axis indexing
463 (black numbers). However, as reported in the stereographic projections, EBSD gives consistent and
464 useful information about the crystal orientation relationship.

465

466 Figure 5. Raman spectrum of röntgenite showing the main vibrational modes of CRFC.

467

468 Figure 6. $\nu_1(\text{CO}_3)$ intensity variation in röntgenite as a function of the crystal orientation and laser
469 polarization.

470

471 Figure 7. a) to (f) Symmetric stretching vibration [$\nu_1(\text{CO}_3)$] in the different polysomes, from the poorest
472 Ca-phase bastnäsite (a), nominally Ca-free, to the richest Ca-phase synchysite with an ideal
473 Ca/(Ca+REE) = 0.50 (f). (b) and (c) were obtained on lamellae homogeneous in BSE images and with
474 Ca/(Ca+REE) ratios of 0.23 and 0.27, respectively, close to the B_2S polysome (0.25). Note the strong
475 orientation dependence of the intensity: $\nu_1(\text{CO}_3)$ is maximal when the laser is polarized parallel to the

476 z-axis ($x \begin{pmatrix} z \\ y \end{pmatrix} \bar{x}$, solid line) and minimal when the laser is polarized perpendicular to the z-axis
477 ($x \begin{pmatrix} y \\ z \end{pmatrix} \bar{x}$, dotted line).

478

479 Figure 8. a) Recurrent microstructure in CRFC from Malawi (sample 9c2), made of dense stacking
480 faults. b) Ordered region of bastnäsite as seen down [010] and related SAED pattern (c).

481

482 Figure 9. Ordered region of parisite (free of compositional faults) as seen down [100] and
483 corresponding SAED pattern (b).

484

485 Figure 10. a) Lamella ~140 nm thick with a *c*-spacing of ~38 Å, consistent with the B_2S polysome.
486 Some stacking faults delimiting the ordered region are indicated by arrows. b) 00*l* row of parisite as
487 compared to the 00*l* row of the B_2S polysome (c) to emphasize the different periodicity of the 002 half-
488 cell. (d) SAED pattern of a further polysome with 001 periodicity of ~34 Å, consistent with B_5S , whose
489 structure, however, needs to be confirmed.

490

491 Figure 11. a) Long range polytype with a repeat distance of ~32 nm (the periodic region extends
492 beyond the observed field of view, up to ~500 nm in total). b) Related SAED pattern. The supercell
493 reflections cannot be resolved, because they are too weak and superposed. The strongest subcell
494 reflections showing a periodicity of ~53 Å (c), whose intensity is further modulated at ~5 Å (brace),
495 suggest a main building block of ~53 Å based on single *B*-layers, which we may tentatively indicate as
496 the thick, darker lamellae in (a) (arrows).

497

498 Figure 12. SAED patterns of parisite-(Ce) structures along $[1\bar{1}0]$: a) Ni et al. (2000); b) Capitani (2019)

499 (both are simulations obtained with the CrystalMaker® X software); c) experimental pattern of the new
500 parisite polymorph detected in this study; inset: zooming of the 11*l* row to highlight the ~56 Å
501 periodicity along *c**, which distinguishes the last from the former two structures (~28 Å), suggesting a
502 new polymorph with a double *c* parameter and a stacking of four *BS* single units (~14 Å).

503

504 Figure 13. BF-STEM images (top) and corresponding compositional line scans (bottom) across a thick
505 lamella within parisite (a) and disordered bastnäsite (b). Note the Ca decrease and the Ce increase at the
506 lamella in parisite and the Ca-Ce inverse correlation in bastnäsite.

507

508 Figure 14. a) HRTEM image of bastnäsite down [010] (SAED pattern similar to Fig. 8c) including
509 some compositional faults (CF, arrows). b) Fourier filtered image of the rectangular area in (a). The
510 unit-cell-scale analysis reveals that these CF can be explained by the insertion of single *B*₂*S* and *B*₃*S*
511 slabs with thickness along *c* of ~19 and ~24 Å, respectively. Other than affecting the slab thickness
512 (approximate values in Å on the right), the CF causes a shift on the (001) plane (*s* = straight, *l* = left, *r*
513 = right shift).

514

515 Figure 15. 1091 cm⁻¹/1081 cm⁻¹ intensity ratio for röntgenite (Roe), parisite (Par) and *B*₂*S* for **E // z**(a)
516 and **E ⊥ z** (b).

517

518 Figure 16. Calculated mineral–fluid equilibria at 300 and 1 kbar for the stability of bastnäsite-(Ce) and
519 parisite-(Ce) as a function of *a*F⁻ and *a*CO₃²⁻ (Gysi and Williams-Jones, 2015).

Table 1.

Mineral phase	EDS (this study)	WDS (Guastoni et al., 2009)
Bastnäsite	$(\text{Ce}_{0.52}\text{La}_{0.27}\text{Nd}_{0.13}\text{Pr}_{0.04}\text{Sm}_{0.01}\text{Gd}_{0.01})_{0.98}$ $(\text{CO}_3)\text{F}_{0.63}$	$(\text{Ce}_{0.51}\text{La}_{0.32}\text{Nd}_{0.09}\text{Y}_{0.01}\text{Pr}_{0.04}\text{Sm}_{0.01})_{0.98}$ $(\text{CO}_3)(\text{F}_{0.95}\text{OH}_{0.07})_{1.02}$
Parisite	$\text{Ca}_{0.96}(\text{Ce}_{1.04}\text{La}_{0.56}\text{Nd}_{0.27}\text{Y}_{0.01}\text{Pr}_{0.09}\text{Sm}_{0.02}\text{Gd}_{0.01})_{2.00}$ $(\text{CO}_3)_3\text{F}_{1.33}$	$\text{Ca}_{0.92}(\text{Ce}_{1.03}\text{La}_{0.53}\text{Nd}_{0.27}\text{Y}_{0.04}\text{Pr}_{0.10}\text{Sm}_{0.04})_{2.01}$ $(\text{CO}_3)_3(\text{F}_{1.70}\text{OH}_{0.30})_2$
Synchysite	$\text{Ca}_{1.04}(\text{Ce}_{0.35}\text{La}_{0.17}\text{Nd}_{0.13}\text{Y}_{0.21}\text{Pr}_{0.03}\text{Sm}_{0.02}\text{Gd}_{0.03})_{0.94}$ $(\text{CO}_3)_2\text{F}_{0.97}$	$\text{Ca}_{0.99}(\text{Ce}_{0.42}\text{La}_{0.22}\text{Nd}_{0.13}\text{Y}_{0.19}\text{Pr}_{0.04}\text{Sm}_{0.03}\text{Th}_{0.01})_{1.04}$ $(\text{CO}_3)_2(\text{F}_{0.79}\text{OH}_{0.21})_1$

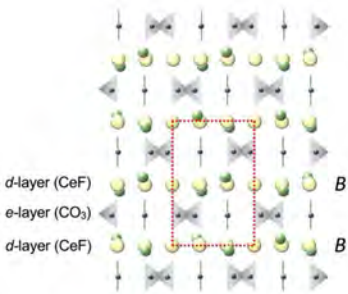
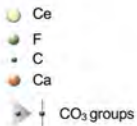
Table 2.

Mode	Bastnäsite	Intermediate polysomes			Synchysite	
ν_1 - symmetric stretching	$\sim 1095 \text{ cm}^{-1}$	$\sim 1081 \text{ cm}^{-1}$	$\sim 1091\text{-}1095 \text{ cm}^{-1}$	$\sim 1099 \text{ cm}^{-1}$	$\sim 1081 \text{ cm}^{-1}$	$\sim 1099 \text{ cm}^{-1}$
ν_2 - out-of-plane bending	$\sim 870 \text{ cm}^{-1}$					
ν_3 - antisymmetric stretching	$\sim 1440 \text{ cm}^{-1}$					
ν_4 - in-plane bending	$665\text{-}754 \text{ cm}^{-1}$					

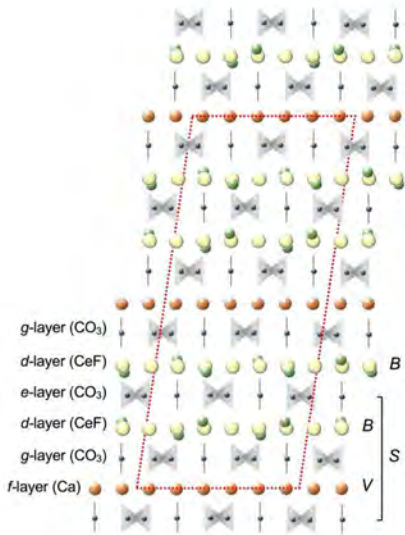
Table 3

	Mineral section	Beam direction	E polarization	Porto's notation
1	yz	x	z	$x \begin{pmatrix} z \\ y \end{pmatrix} \bar{x}$
2	yz	x	y	$x \begin{pmatrix} y \\ z \end{pmatrix} \bar{x}$
3	yx	z	y	$z \begin{pmatrix} y \\ x \end{pmatrix} \bar{z}$
4	yx	z	x	$z \begin{pmatrix} x \\ y \end{pmatrix} \bar{z}$

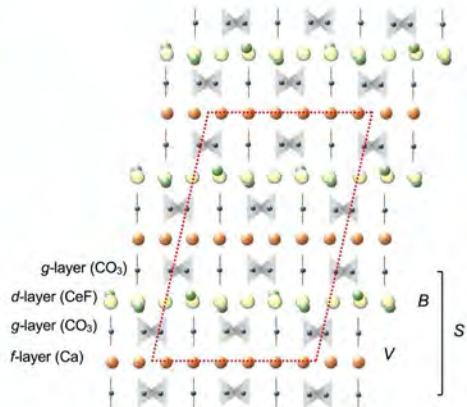
Figure 1



bastnäsite ($B_2 - BB$)



parisite ($BS - VBBVBB$)



synchysite ($S - VB$)

Figure 2

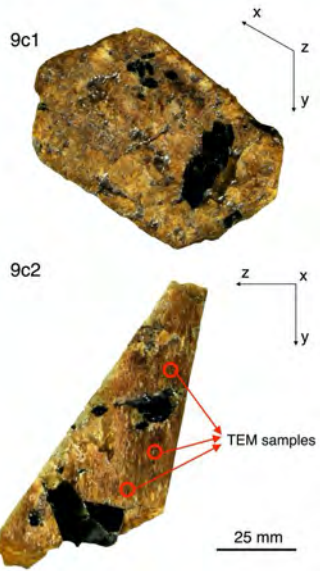
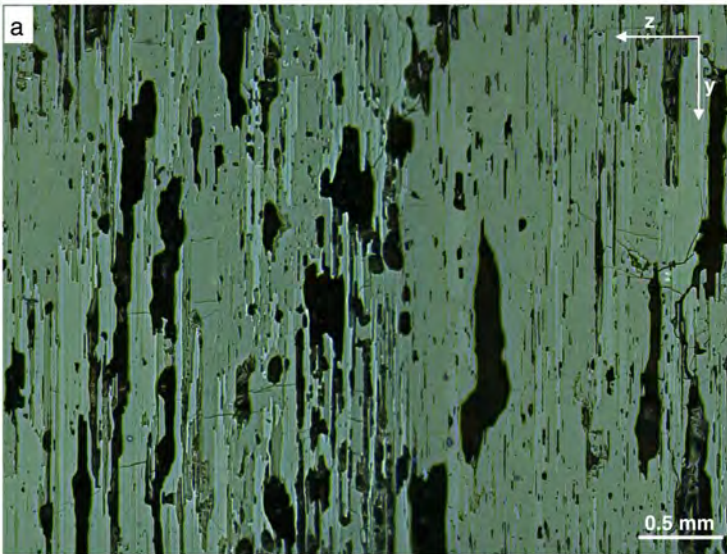


Figure 3

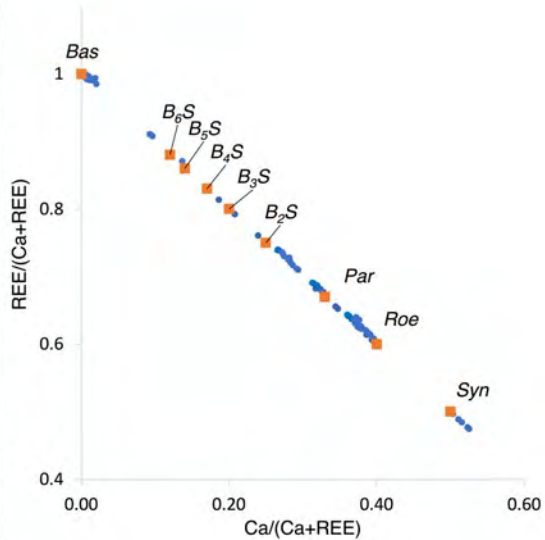
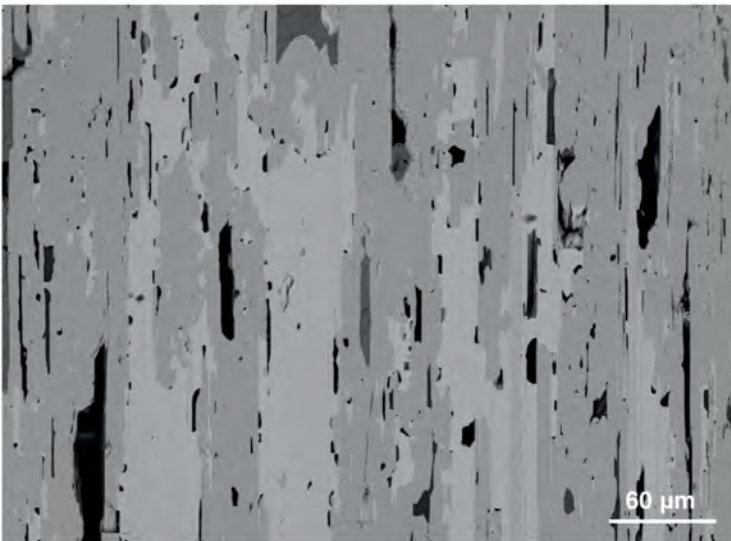
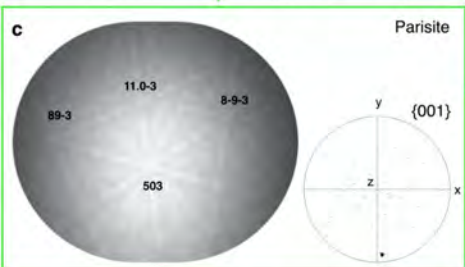
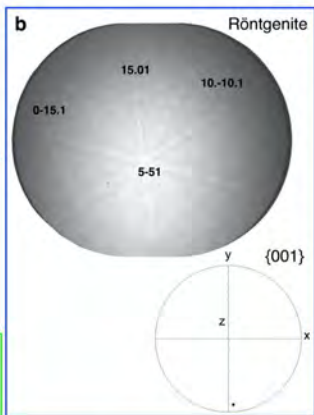
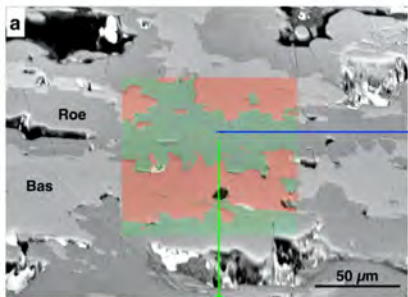


Figure 4



- Bastnäsite
- Parisite
- Röntgenite
- Synchronsite

Figure 5

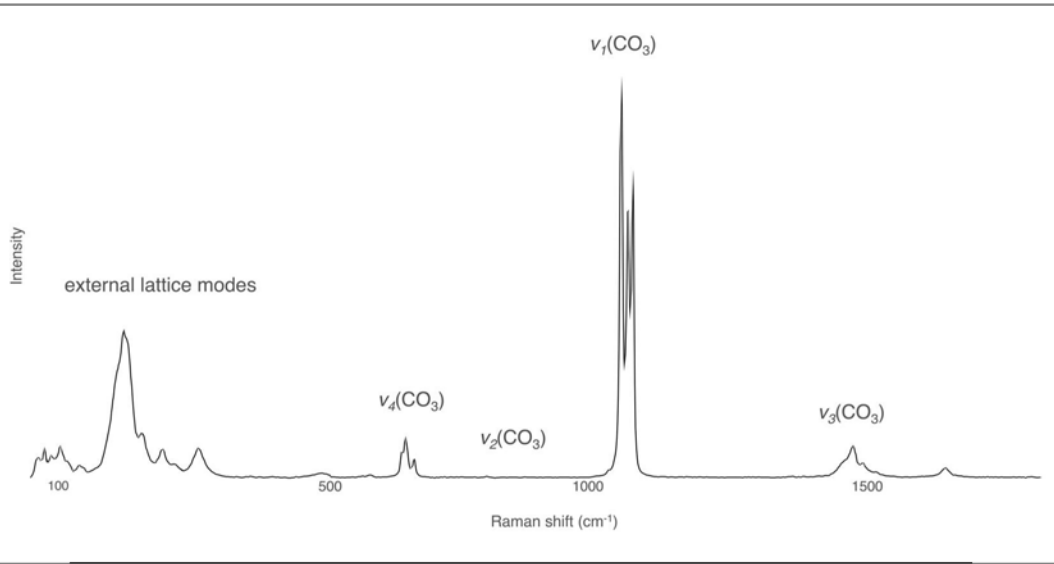


Figure 6

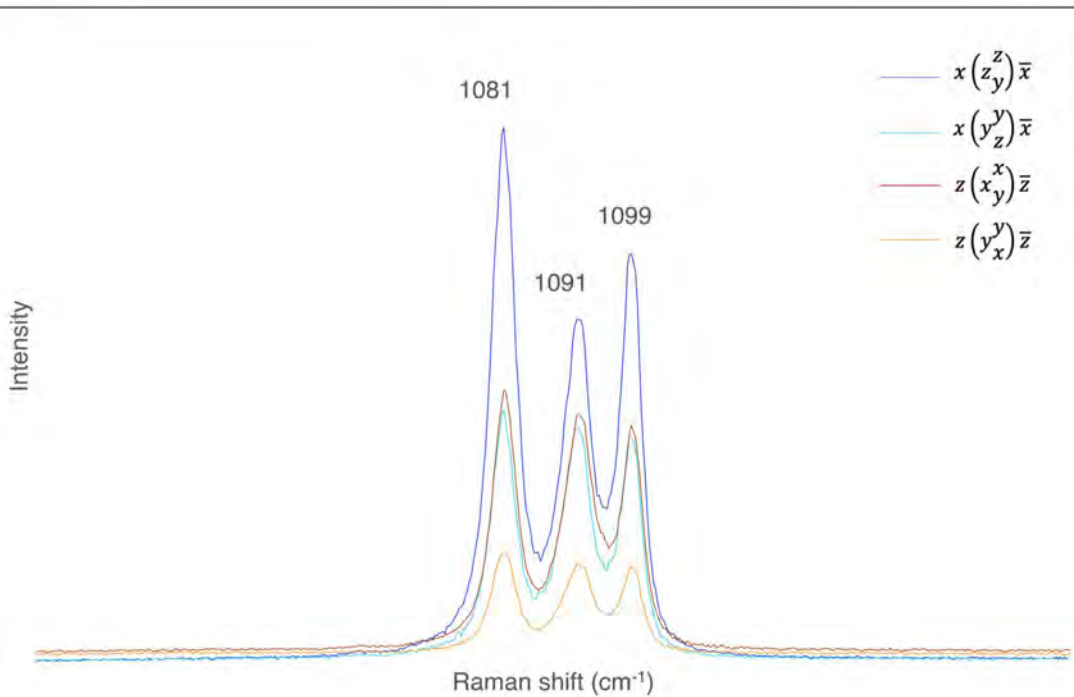


Figure 7

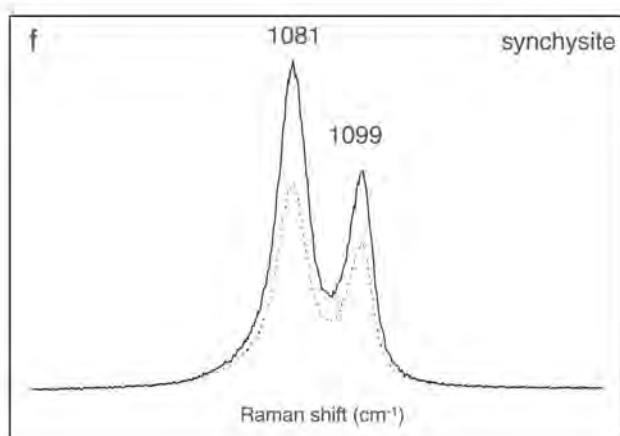
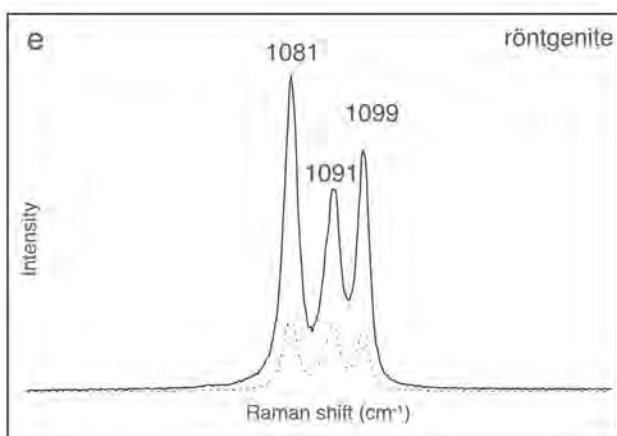
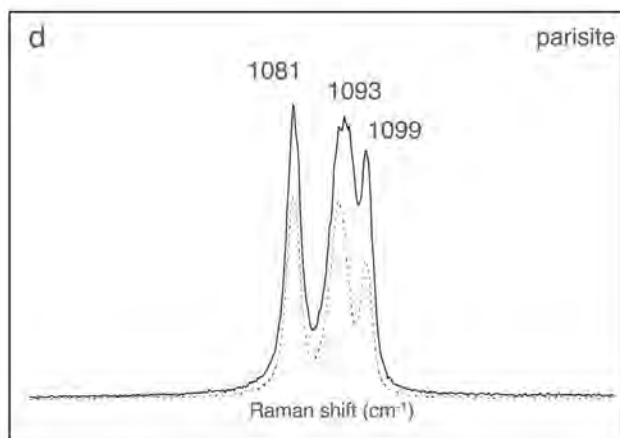
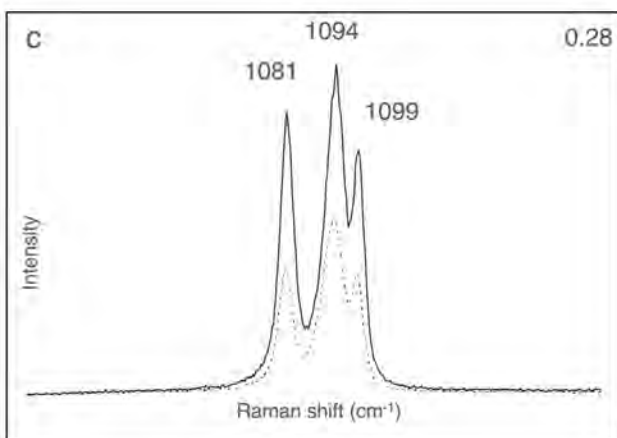
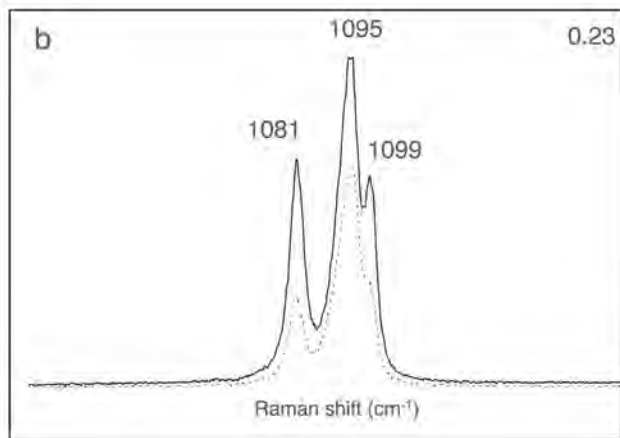
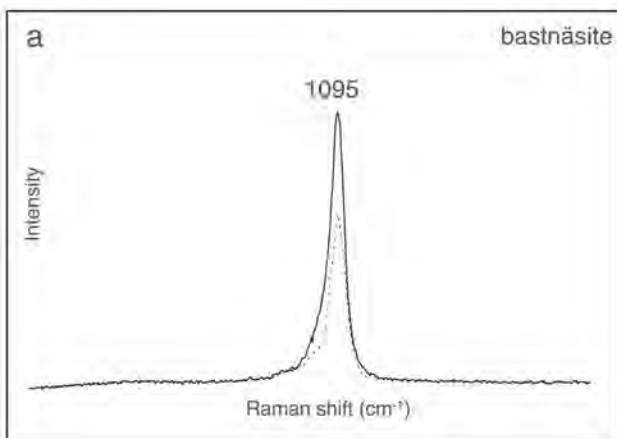


Figure 8

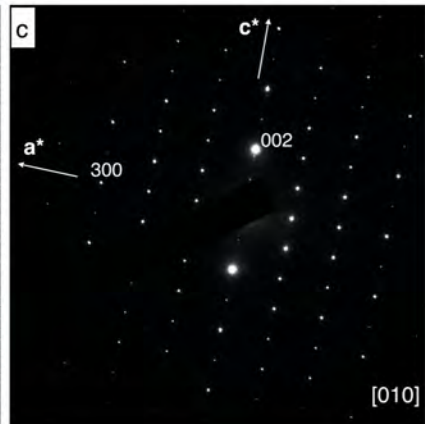
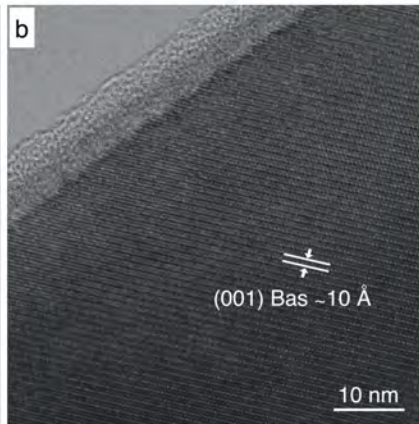
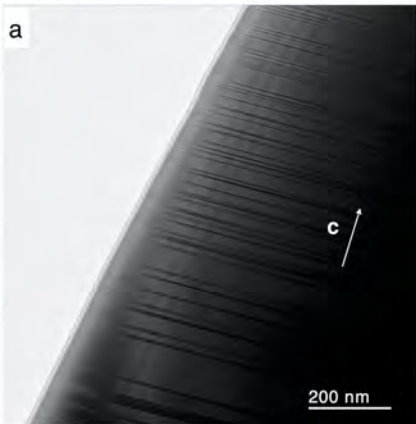


Figure 9

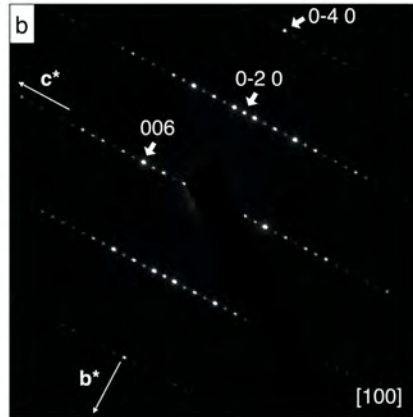
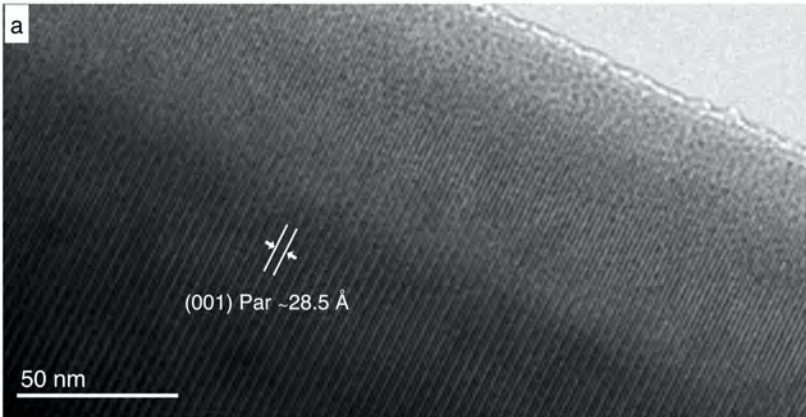


Figure 10

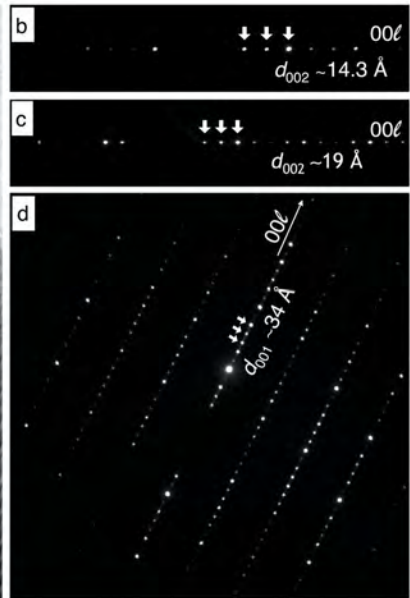
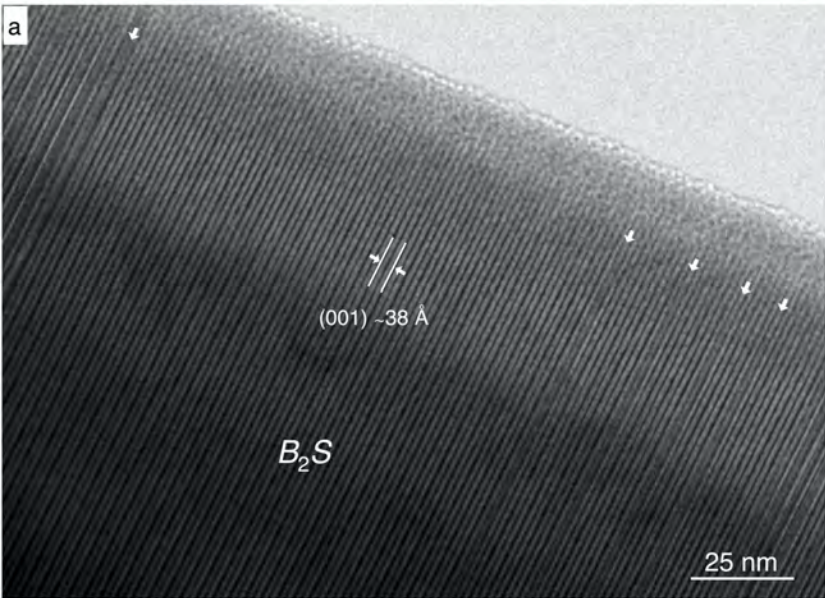


Figure 11

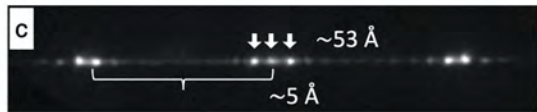
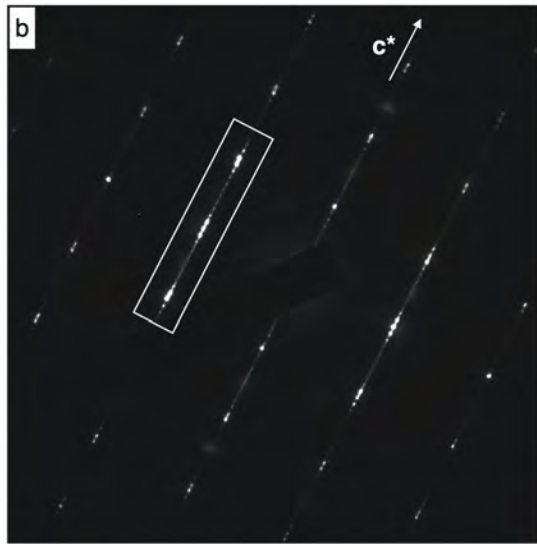
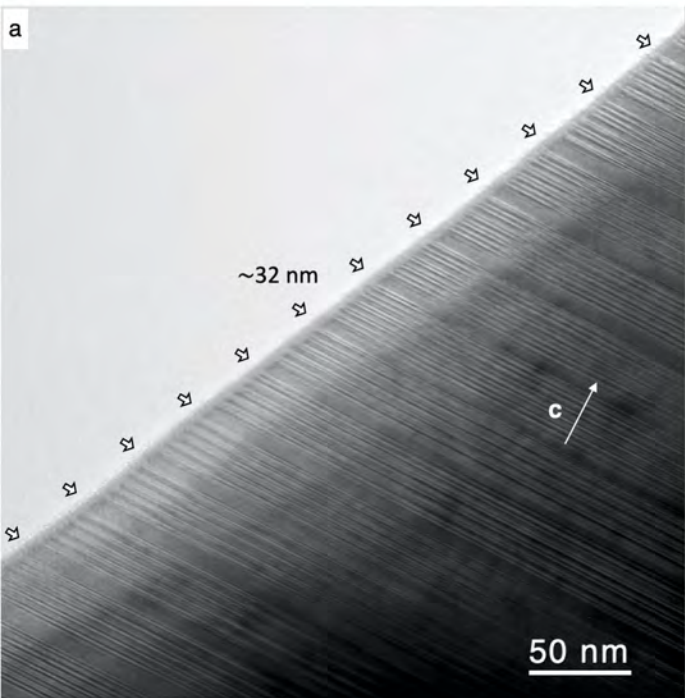


Figure 12

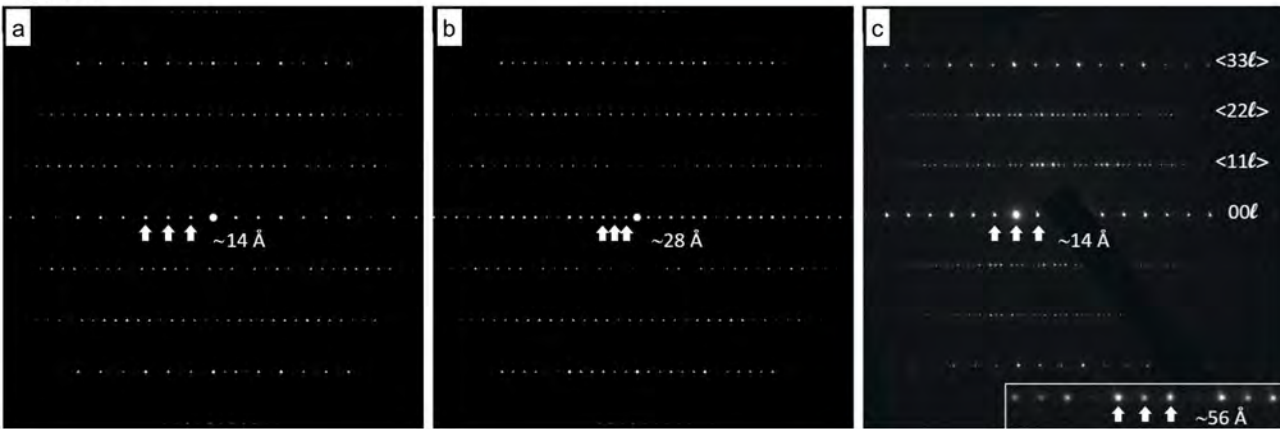


Figure 13

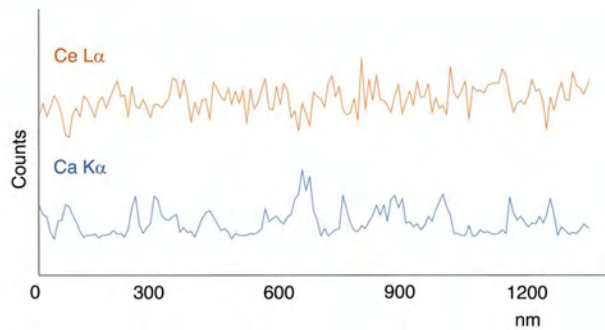
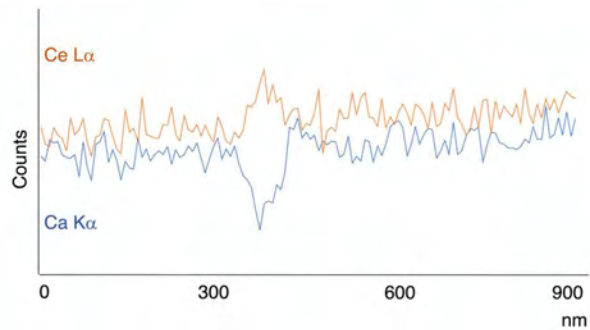
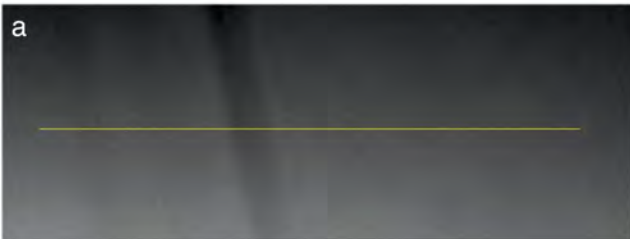


Figure 15

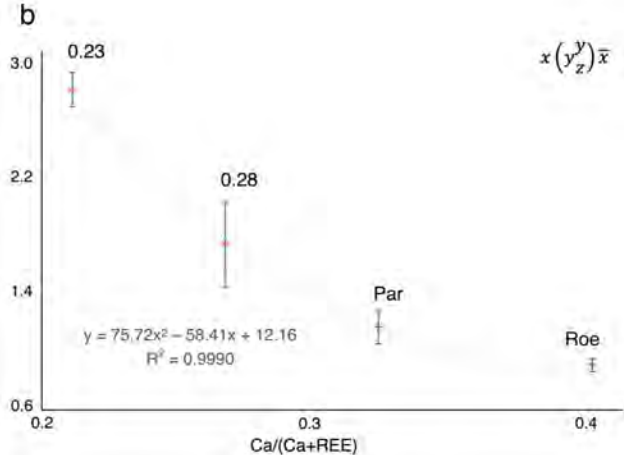
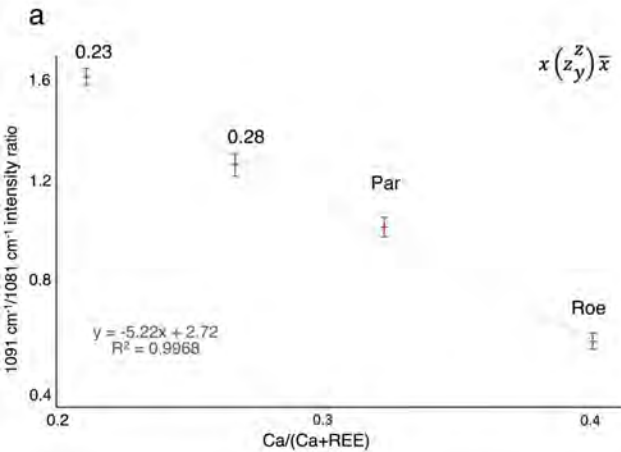


Figure 16

